Cambridge University Press
9780521760515 – Heliophysics: Space Storms and Radiation: Causes and Effects
Edited by Carolus J. Schrijver , George L. Siscoe
[Plate Section]

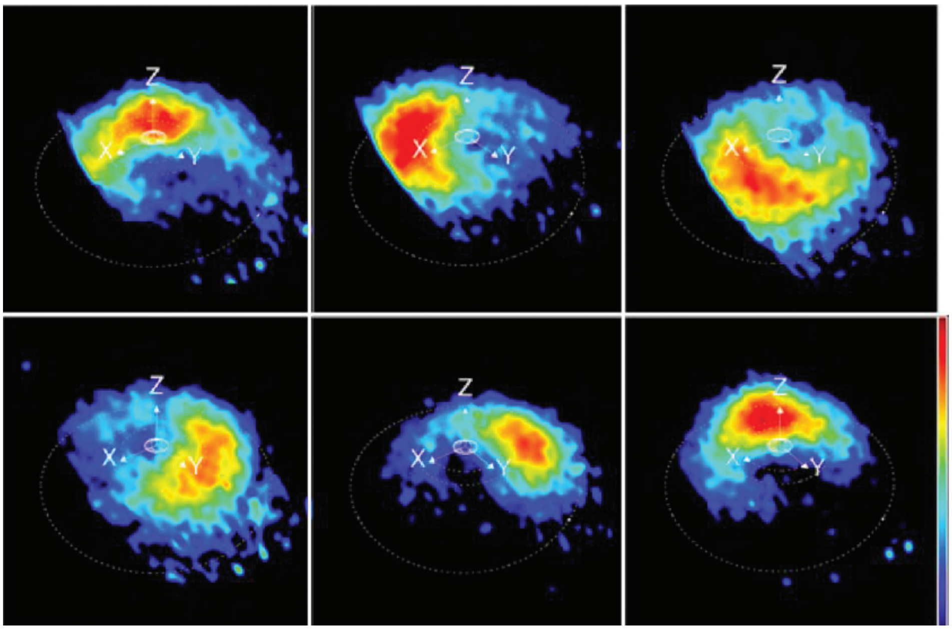

Plate 1 (Fig. 3.23). Neutral-hydrogen (20–50 keV) images of Saturn's ring current taken with the INCA sensor on Cassini at 2.13-hour intervals showing counterclockwise rotation in the plasma. (Courtesy S. M. Krimigis.)

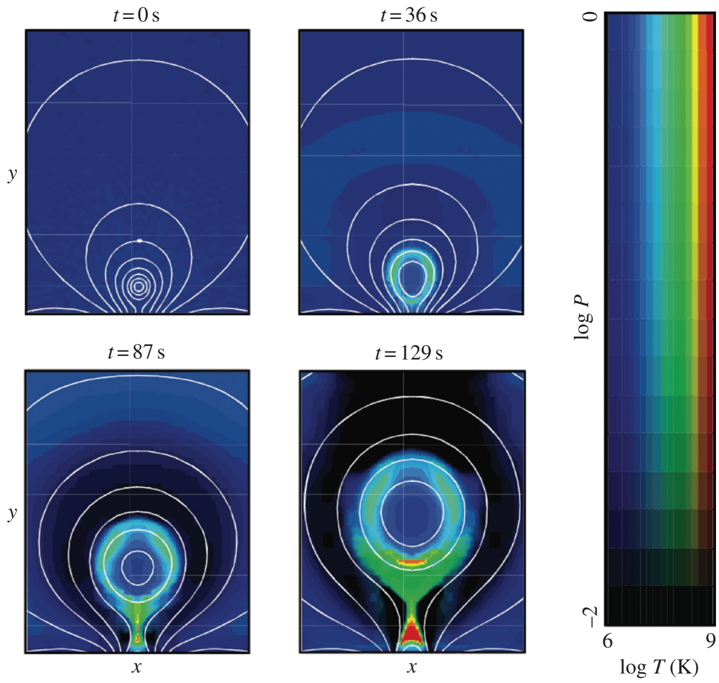

Plate 2 (Fig. 6.12). Numerical simulation of an erupting flux rope. The color hue indicates the temperature, while the color intensity indicates the pressure. The white lines are contours of the flux function.

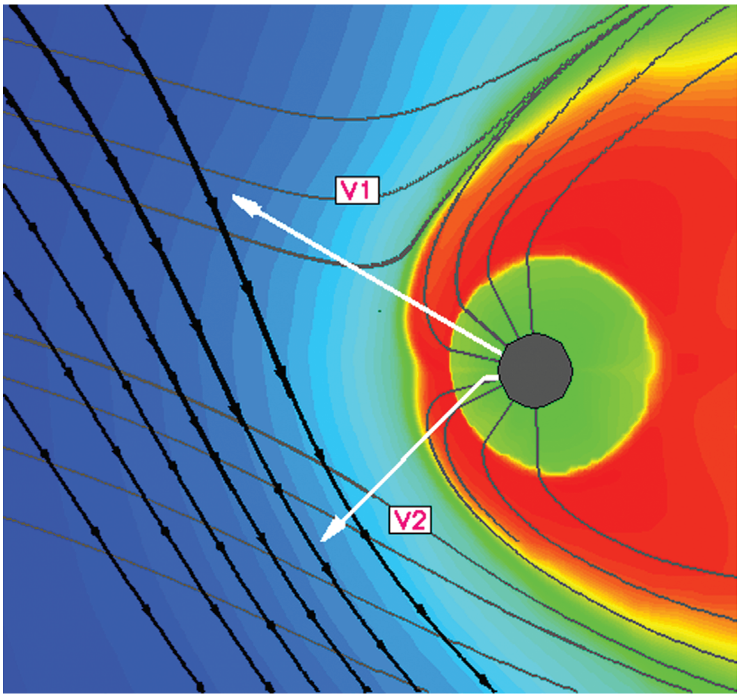

Plate 3 (Fig. 7.4). Meridional cut from a heliosphere simulation including the plasma and the neutral H atoms (Opher, 2009). The contours are the plasma temperature. The blue region is the region beyond the heliopause; the red, the heliosheath; and the central green area is the region upstream of the solar-wind termination shock. The black lines are the interstellar magnetic field and the grey lines are the plasma streamlines. The (projected) trajectories of the Voyager 1 and 2 spacecraft are also indicated.

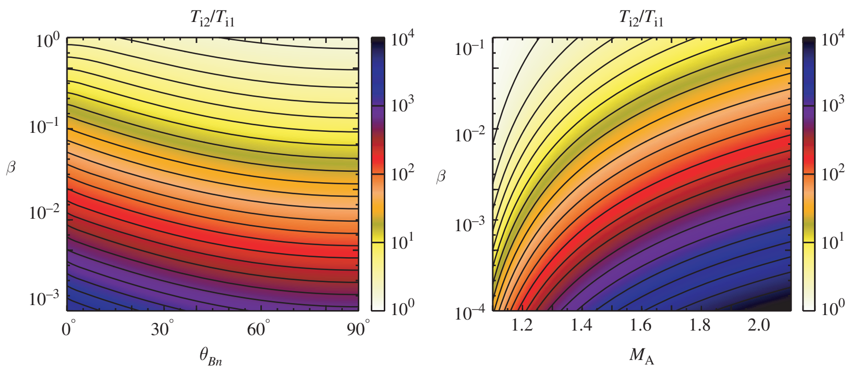

Plate 4 (Fig. 8.1). Iso-contours of shock heating, expressed as the ratio between downstream to upstream ion temperature T_{i2}/T_{i1}, as a function of shock-normal angle θ_{Bn} (fixed $M_A = 2$) and Alfvén Mach number M_A (fixed $\theta_{Bn} = 45^\circ$) for low β plasmas. Derived from standard Rankine–Hugoniot conditions for fast shocks, assuming a specific heat ratio $\gamma = 5/3$. The graphs show that for a wide range of angles there can be very substantial downstream heating at sufficiently low plasma β, as present in much of the solar corona. Such extreme heating may help form a seed population for further acceleration.

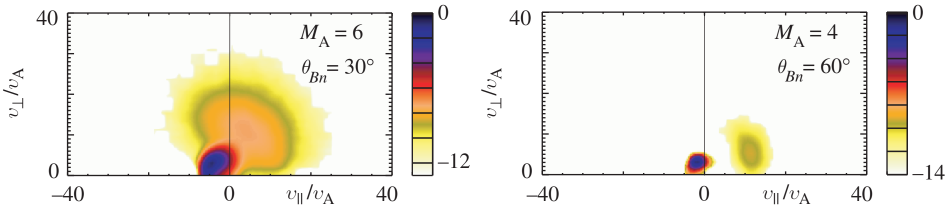

Plate 5 (Fig. 8.5). Sketch of upstream proton distributions (perpendicular and parallel to the ambient magnetic field) in the shock frame from planar, 2D hybrid shock simulations at quasi-parallel ($\theta = 30^\circ$) and oblique ($\theta = 60^\circ$) angles. As in many documented observations of the Earth's bow shock and at sufficiently high Mach number IP shocks, at quasi-parallel shock-normal angles, protons can not only easily travel upstream and generate waves, but they also easily scatter in these self-generated waves to form a diffuse distribution that forms a contiguous cloud of both upstream ($v_\parallel > 0$) and downstream ($v_\parallel < 0$) directed particles. Conversely, at oblique shocks, only a highly dilute upstream-propagating beam with enhanced perpendicular energy is found, and even that can only be seen with very good statistics, in simulations. Unlike the quasi-parallel shock, a higher Mach number does not help initially, but typically makes it more difficult for ions to make it upstream in the first place.

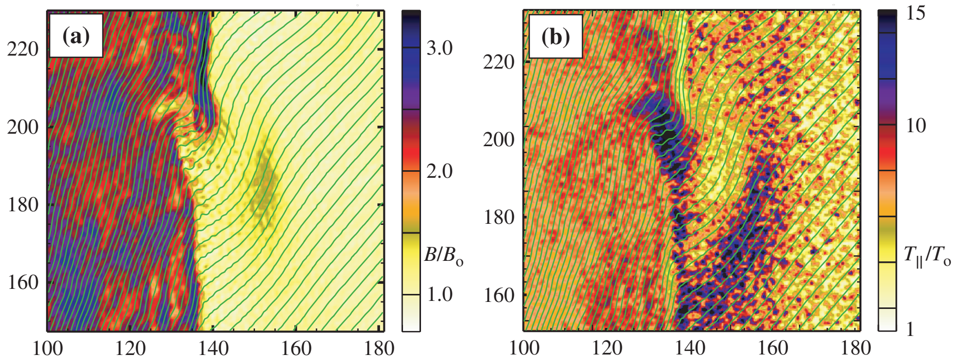

Plate 6 (Fig. 8.6). Magnetic field line contours and (a) total magnetic field, and (b) parallel temperature $T_\parallel$ normalized to upstream in a subset of a 2D hybrid simulation of an oblique shock ($\theta = 50^\circ$). (From Krauss-Varban *et al.*, 2008.) It can be seen how compressional waves generated by dilute beams disrupt the shock and change the local θ_{Bn}, in turn allowing more upstream wave and particle production than expected at the oblique shock. This process appears to enhance upstream energetic proton fluxes by two to three orders of magnitude.

Cambridge University Press
9780521760515 – Heliophysics: Space Storms and Radiation: Causes and Effects
Edited by Carolus J. Schrijver , George L. Siscoe
[Plate Section]

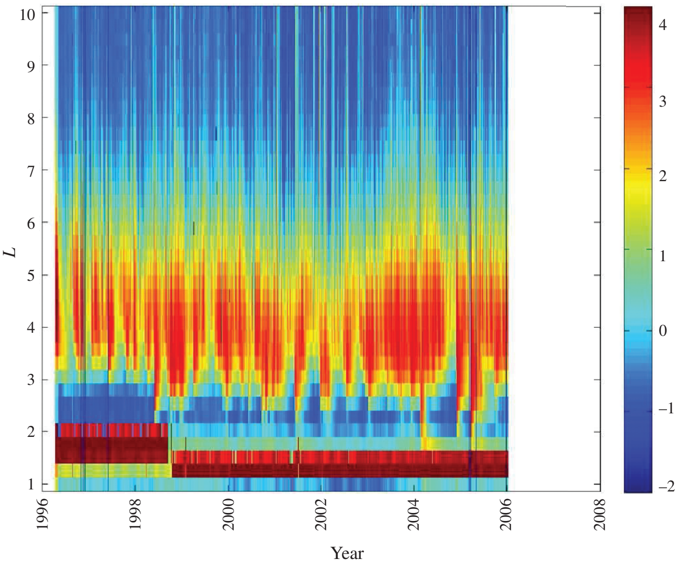

Plate 7 (Fig. 11.5). Radiation belt electron flux (^{10}log(counts/s)) as measured by the Proton Electron Telescope (PET) Elo channel that measures electrons with energies $>$ 1.5 MeV on the SAMPEX satellite. The data are averaged in 0.25L and 1 day bins.

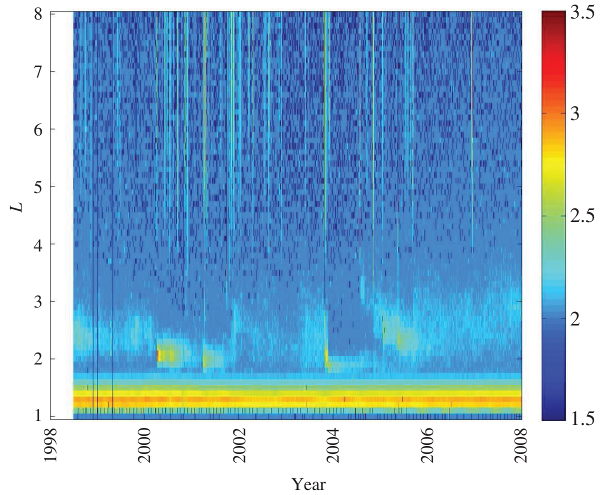

Plate 8 (Fig. 11.6). Radiation belt proton flux (number per cm^2 s str on a logarithmic scale) from the SEM-2 instrument that measures protons with energies between 2.5 and 6.9 MeV on the NOAA-15 satellite. The data are averaged in 0.2L and 1 day bins.

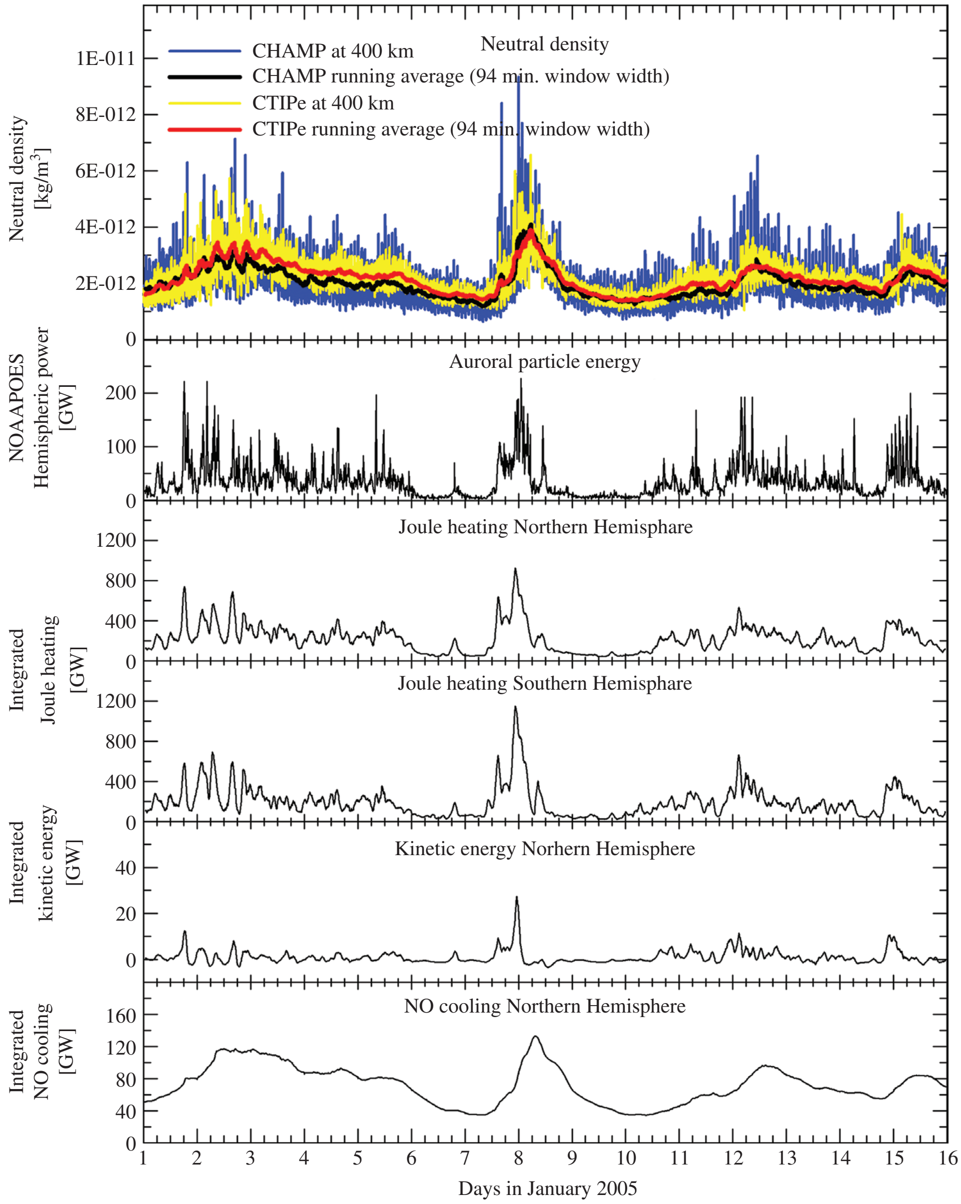

Plate 9 (Fig. 12.1). Ionospheric properties during a geomagnetic storm. The upper panel shows a comparison of CHAMP neutral density measurements at 400 km altitude with a numerical simulation, for a stormy period in January 2005. The lower panels show, from top to bottom, estimates of auroral power, Joule heating in the Northern and Southern Hemispheres, kinetic energy deposition, and nitric oxide infrared cooling rates. (Courtesy of M. Fedrizzi.)

Cambridge University Press
9780521760515 – Heliophysics: Space Storms and Radiation: Causes and Effects
Edited by Carolus J. Schrijver , George L. Siscoe
[Plate Section]

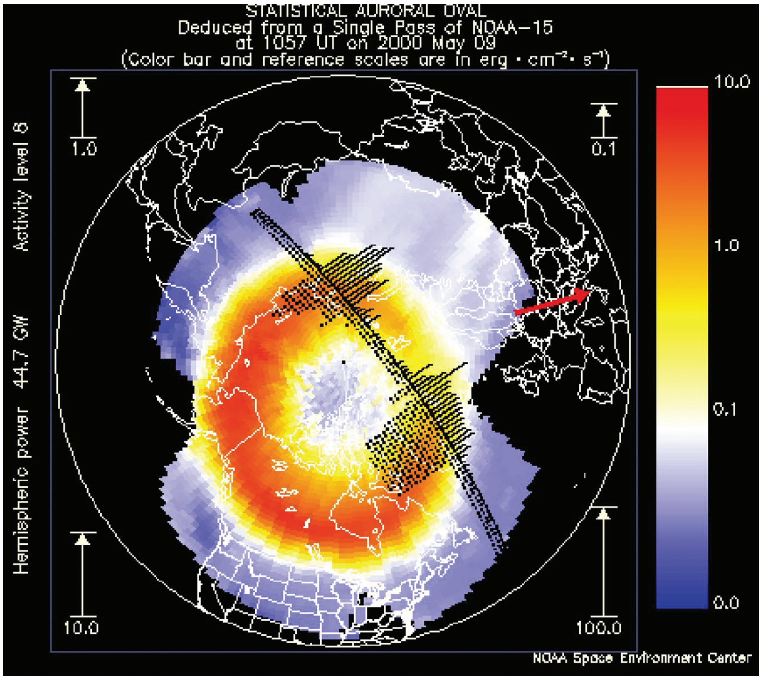

Plate 10 (Fig. 12.2). Statistical pattern of auroral energy input derived from TIROS/NOAA satellite data during a single transit of the polar region. (From Evans *et al.*, 1988.)

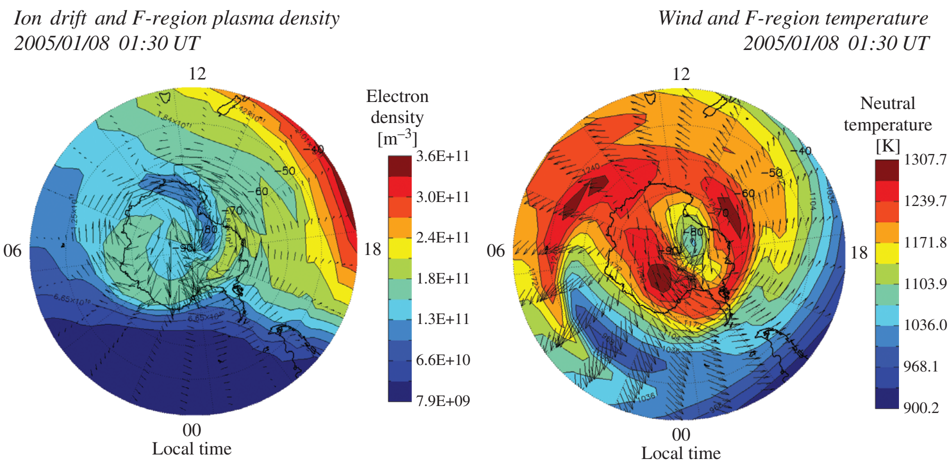

Plate 11 (Fig. 12.3). Simulated response of the F-region plasma densities (left) and neutral winds and temperature (right) at the peak of the storm at 1:30 UT on January 8, 2005, in the Southern Hemisphere. Both represent the response in the upper thermosphere and ionosphere at about 300 km altitude. Peak neutral winds are in excess of 800 m/s. (Courtesy of M. Fedrizzi.)

CAMBRIDGE

Cambridge University Press
9780521760515 – Heliophysics: Space Storms and Radiation: Causes and Effects
Edited by Carolus J. Schrijver , George L. Siscoe
[Plate Section]

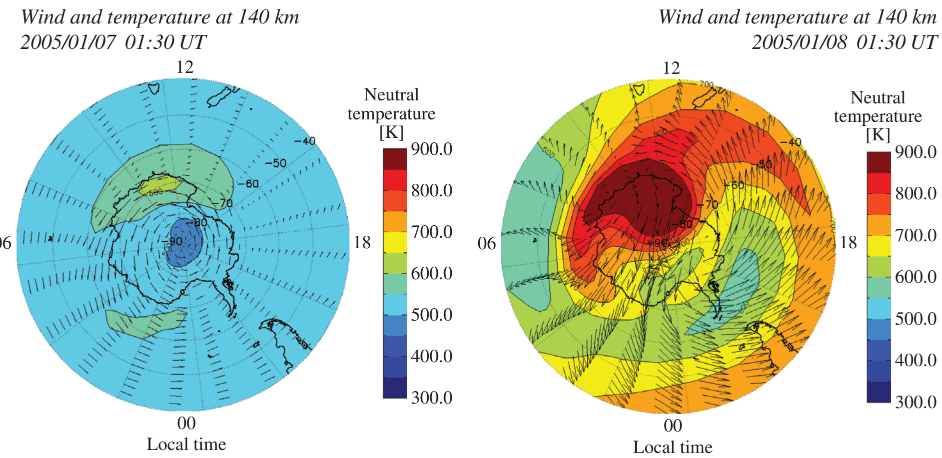

Plate 12 (Fig. 12.4). Neutral winds in the lower thermosphere at around 140 km altitude at the peak of the storm at 1:30 UT on January 8, 2005, in the Southern Hemisphere (right), and at the same UT on the quiet day preceding the storm (left). Winds in the lower thermosphere increase dramatically in response to the storm, but peak magnitudes are about half those at 300 km. Lower thermosphere winds driven by the storm also tend to be slower to dissipate, sometimes acting as a "flywheel" driving Poynting flux upward from the thermosphere/ionosphere to the magnetosphere. (Courtesy of M. Fedrizzi.)

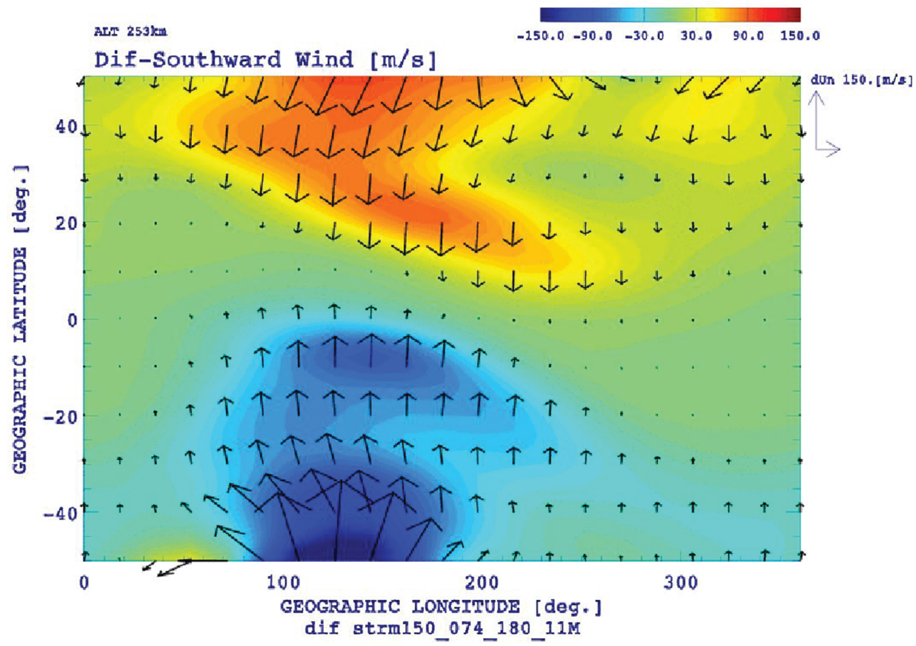

Plate 13 (Fig. 12.5). Simulation of the response of the neutral winds at mid and low latitudes at 250 km altitude, shortly after a sudden increase in high-latitude Joule heating. The region within 50° of the geographic equator is shown at 15 UT, three hours after the increase in high-latitude magnetospheric forcing, equivalent to a $K_p \sim 7$. Wind surges of ~150 m/s are produced, mainly on the night side.

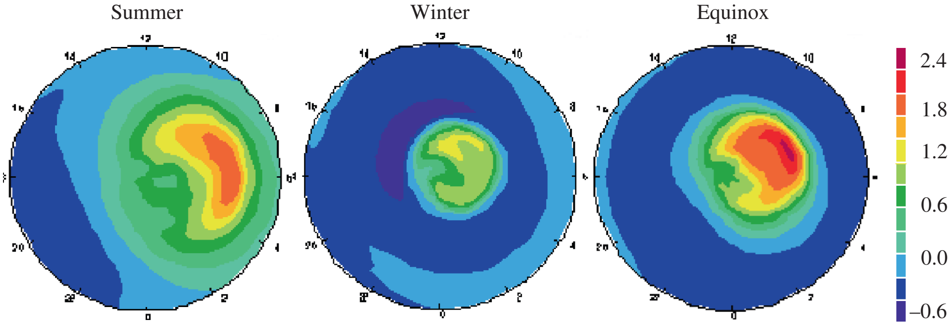

Plate 14 (Fig. 12.6). Numerical simulations of the equatorward extent of the "composition bulge" for equivalent storms in the Northern Hemisphere for summer (left), winter (middle), and equinox (right). The seasonal circulation assists the transport to low latitudes in the summer hemisphere and inhibits the transport in winter.

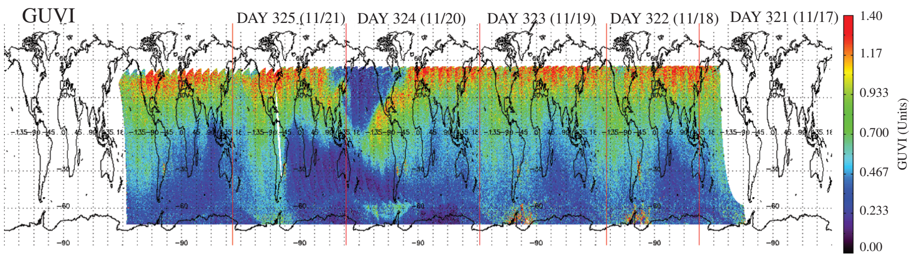

Plate 15 (Fig. 12.7). Changes in the column-integrated O/N_2 ratio during the November 2003 Halloween storm. (From review by Crowley and Meier, 2008; after Meier *et al.*, 2005.) The data are from the GUVI instrument on the TIMED satellite (Paxton *et al.*, 1999). Five days of GUVI data are plotted as individual day-side orbits and assembled as a montage; time runs from right to left. The storm event on day 324 causes a decrease in the column-integrated O/N_2 in both hemispheres. The Southern Hemisphere depletion penetrates further equatorward as expected from the transport effect of the global seasonal circulation.

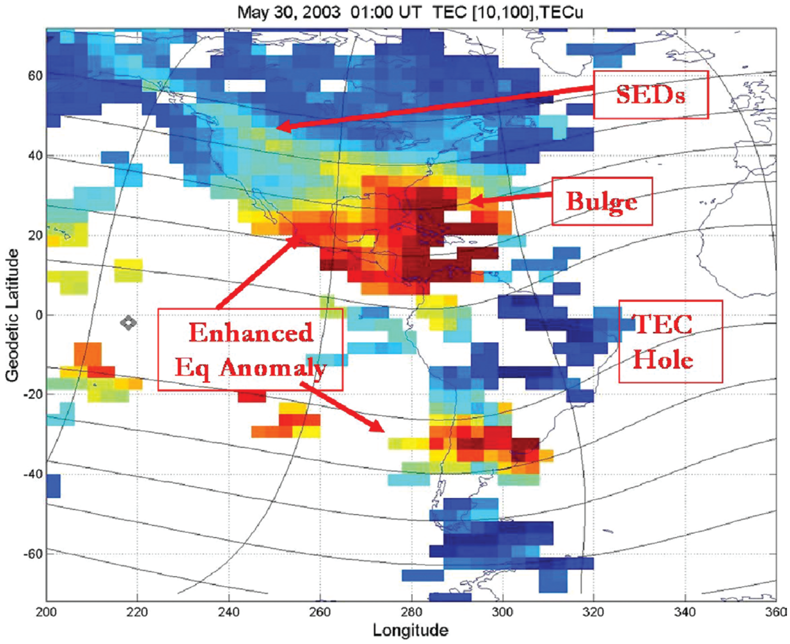

Plate 16 (Fig. 12.9). Illustration of the large enhancement "bulge" in TEC at mid-latitudes during a geomagnetic storm, and showing the plume of plasma (storm-enhanced density, or SED) connecting the bulge to the high latitudes. (Courtesy of J. Foster.)

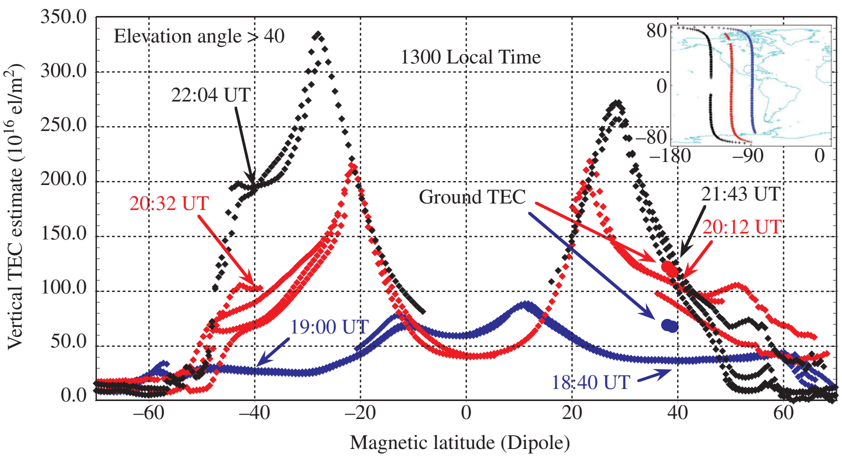

Plate 17 (Fig. 12.10). Order of magnitude increases in over-the-satellite electron content (OSEC) above 400 km during the Halloween storm of October 28, 2003, as measured by the CHAMP satellite. (From Sparks *et al.*, 2005; figure updated by A. Mannucci.)

Cambridge University Press
9780521760515 – Heliophysics: Space Storms and Radiation: Causes and Effects
Edited by Carolus J. Schrijver , George L. Siscoe
[Plate Section]

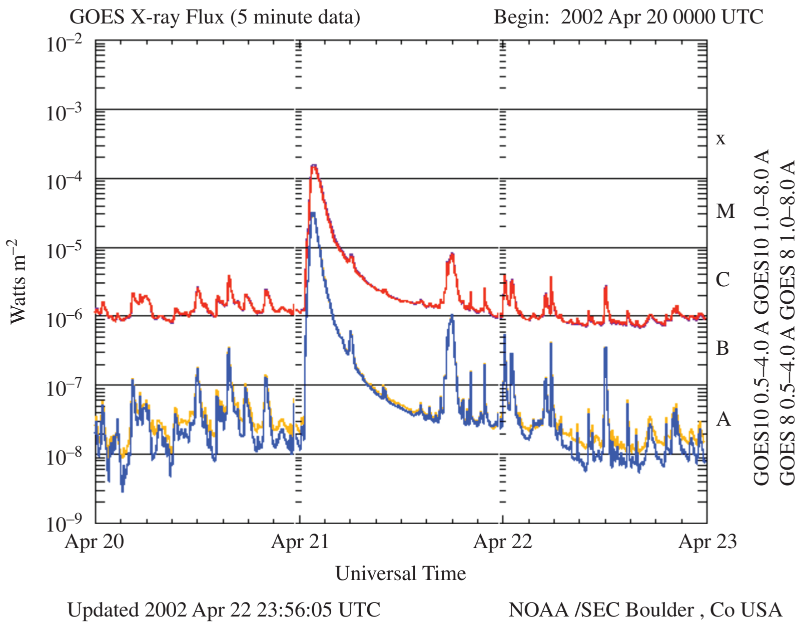

Plate 18 (Fig. 12.13). Example of GOES XRS measurements during a large (X1.5) solar flare.

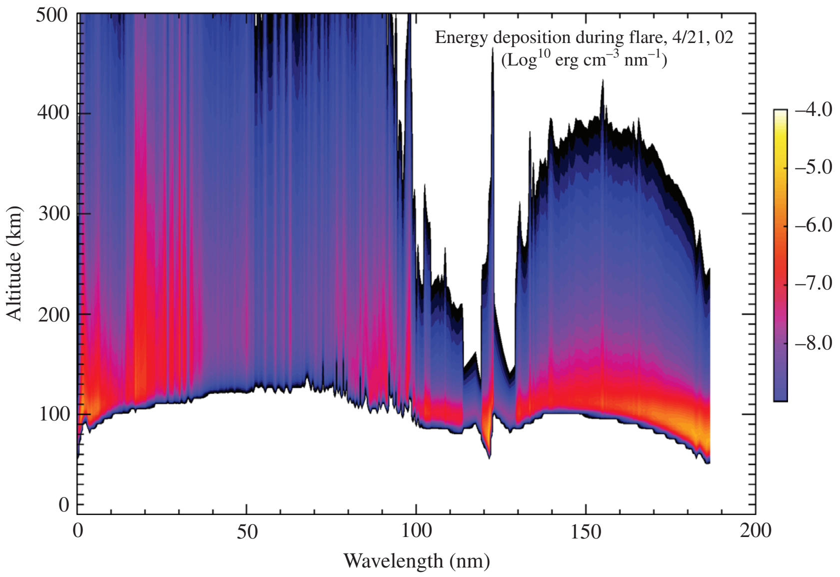

Plate 19 (Fig. 12.17). Energy deposition in the upper atmosphere as a function of wavelength and altitude during a solar flare.

Cambridge University Press
9780521760515 – Heliophysics: Space Storms and Radiation: Causes and Effects
Edited by Carolus J. Schrijver , George L. Siscoe
[Plate Section]

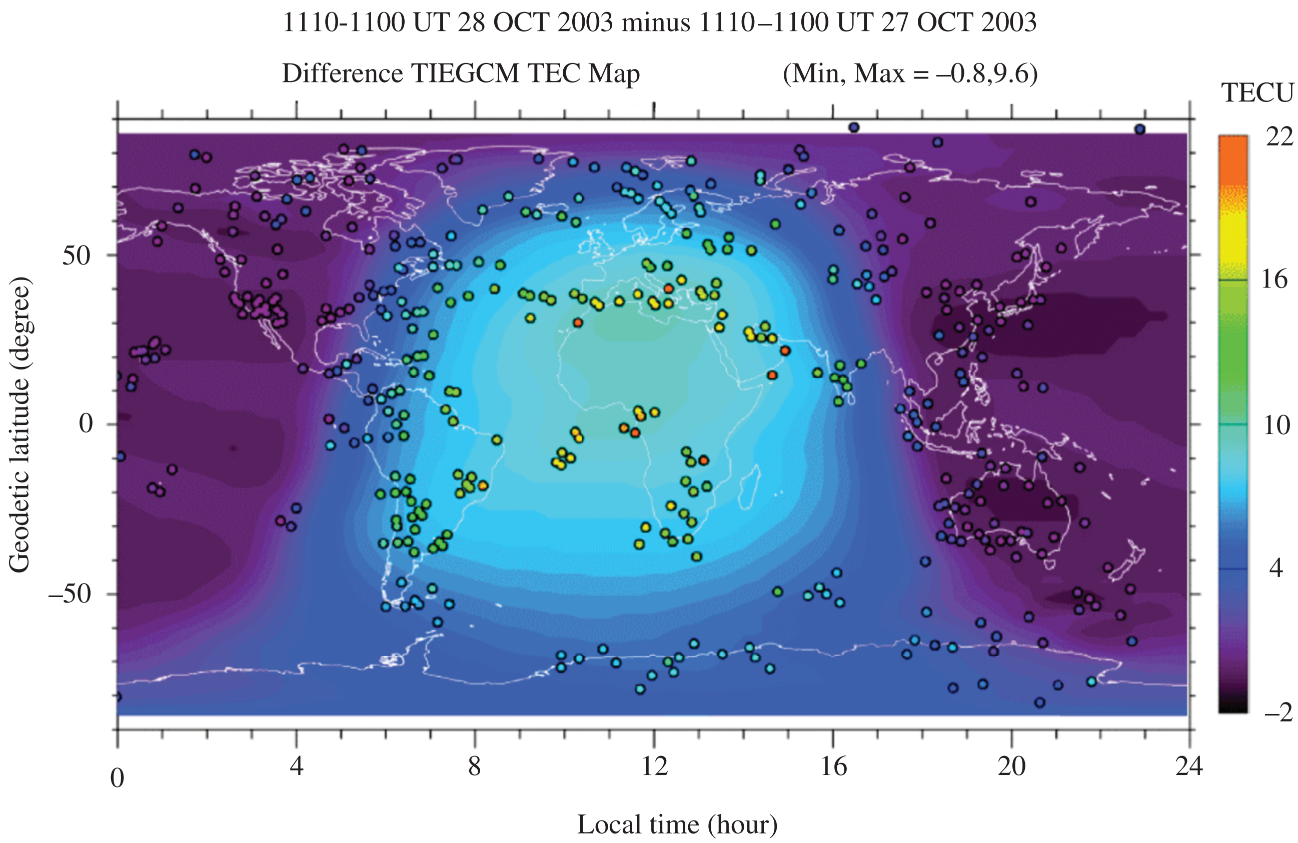

Plate 20 (Fig. 12.19). Comparison of total electron content enhancements during the October 28, 2003 flare, observed by the global network of differential GPS stations, and modeled using the NCAR Thermosphere-Ionosphere-Electrodynamics General Circulation Model (TIE-GCM). Total electron content is the vertically integrated column electron content in units of $10^{16} m^{-2}$.

Cambridge University Press
9780521760515 – Heliophysics: Space Storms and Radiation: Causes and Effects
Edited by Carolus J. Schrijver , George L. Siscoe
[Plate Section]

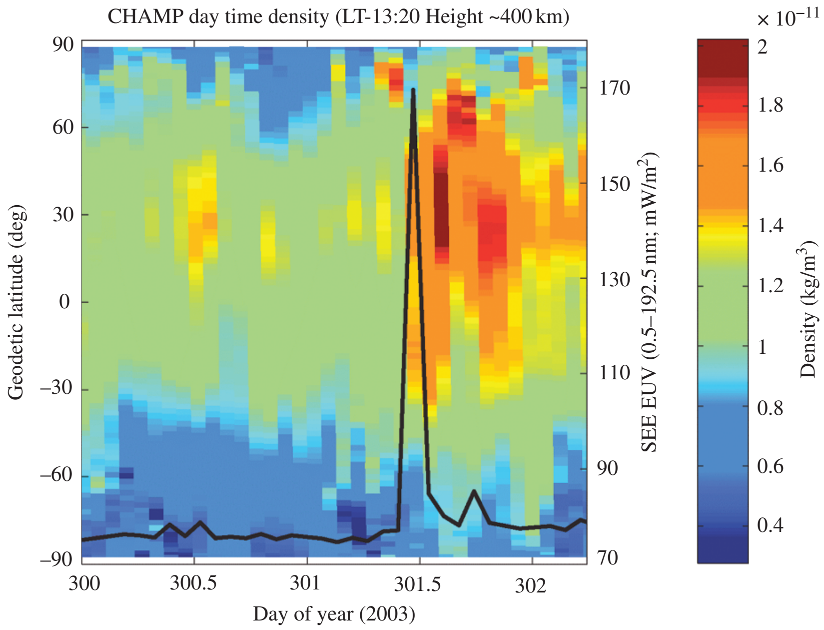

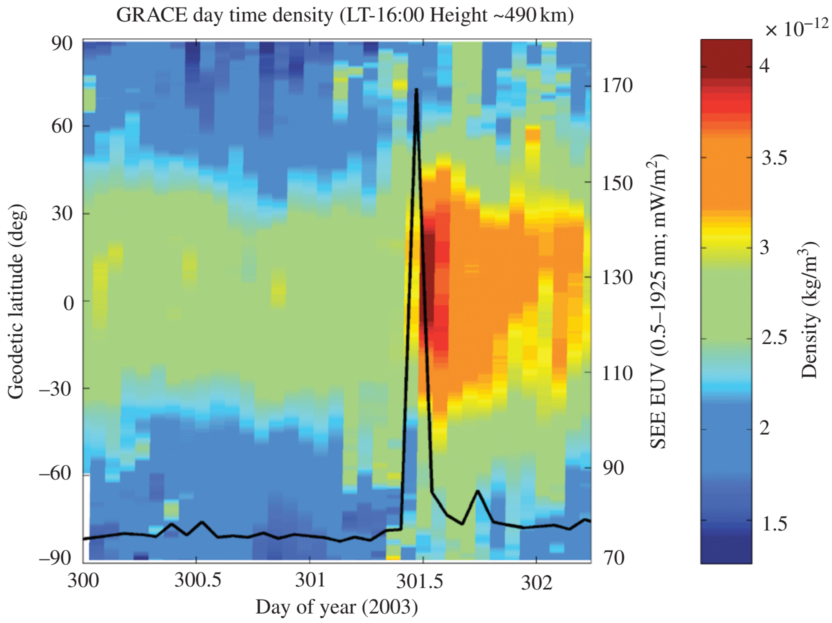

Plate 21 (Fig. 12.20). Thermospheric density enhancements measured by accelerometers on the CHAMP satellite (altitude ∼400 km) and GRACE satellite (altitude ∼490 km) during the October 28, 2003 flare. (Sutton *et al*., 2006.)

